



Universal scaling laws for charge-carrier interactions with quantum confinement in lead-halide perovskites

Philippe Tamarat, Elise Prin, Yuliia Berezovska, Anastasiia Moskalenko, Thi Phuc Tan Nguyen, Chenghui Xia, Lei Hou, Jean-Baptiste Trebbia, Marios Zacharias, Laurent Pedesseau, et al.

► To cite this version:

Philippe Tamarat, Elise Prin, Yuliia Berezovska, Anastasiia Moskalenko, Thi Phuc Tan Nguyen, et al.. Universal scaling laws for charge-carrier interactions with quantum confinement in lead-halide perovskites. *Nature Communications*, 2023, 14 (1), pp.229. 10.1038/s41467-023-35842-4 . hal-03940652

HAL Id: hal-03940652

<https://hal.science/hal-03940652>

Submitted on 20 Jan 2023

HAL is a multi-disciplinary open access archive for the deposit and dissemination of scientific research documents, whether they are published or not. The documents may come from teaching and research institutions in France or abroad, or from public or private research centers.

L'archive ouverte pluridisciplinaire **HAL**, est destinée au dépôt et à la diffusion de documents scientifiques de niveau recherche, publiés ou non, émanant des établissements d'enseignement et de recherche français ou étrangers, des laboratoires publics ou privés.

Universal scaling laws for charge-carrier interactions with quantum confinement in lead-halide perovskites

Received: 9 December 2022

Accepted: 4 January 2023

Published online: 16 January 2023



Philippe Tamarat^{1,2}, Elise Prin^{1,2}, Yulia Berezovska^{3,4}, Anastasiia Moskalenko^{3,4}, Thi Phuc Tan Nguyen⁵, Chenghui Xia^{1,2}, Lei Hou^{1,2}, Jean-Baptiste Trebbia^{1,2}, Marios Zacharias⁶, Laurent Pedesseau⁶, Claudine Katan⁵, Maryna I. Bodnarchuk³, Maksym V. Kovalenko^{3,4}, Jacky Even⁶✉ & Brahim Lounis^{1,2}✉

Lead halide perovskites open great prospects for optoelectronics and a wealth of potential applications in quantum optical and spin-based technologies. Precise knowledge of the fundamental optical and spin properties of charge-carrier complexes at the origin of their luminescence is crucial in view of the development of these applications. On nearly bulk Cesium-Lead-Bromide single perovskite nanocrystals, which are the test bench materials for next-generation devices as well as theoretical modeling, we perform low temperature magneto-optical spectroscopy to reveal their entire band-edge exciton fine structure and charge-complex binding energies. We demonstrate that the ground exciton state is dark and lays several millielectronvolts below the lowest bright exciton sublevels, which settles the debate on the bright-dark exciton level ordering in these materials. More importantly, combining these results with spectroscopic measurements on various perovskite nanocrystal compounds, we show evidence for universal scaling laws relating the exciton fine structure splitting, the trion and biexciton binding energies to the band-edge exciton energy in lead-halide perovskite nanostructures, regardless of their chemical composition. These scaling laws solely based on quantum confinement effects and dimensionless energies offer a general predictive picture for the interaction energies within charge-carrier complexes photo-generated in these emerging semiconductor nanostructures.

Lead halide perovskites have recently emerged as one of the most promising materials for a broad range of applications ranging from photovoltaics to optoelectronics^{1–4} and potential applications as quantum light sources^{5–10}. While intense experimental and theoretical efforts have been made to explore their unique optical and electronic

properties, the physics of band-edge charge complexes (e.g. excitons, trions, biexcitons), whose recombination is at the origin of the luminescence, remains unclear.

For instance, the ordering of bright and dark sublevels in the exciton fine structure is a subject of ongoing debate, though essential

¹Université de Bordeaux, LP2N, Talence F-33405, France. ²Institut d'Optique and CNRS, LP2N, Talence F-33405, France. ³Empa-Swiss Federal Laboratories for Materials Science and Technology, CH-8600 Dübendorf, Switzerland. ⁴Institute of Inorganic Chemistry, Department of Chemistry and Applied Biosciences, ETH Zürich, CH-8093 Zürich, Switzerland. ⁵Univ Rennes, ENSCR, CNRS, ISCR-UMR 6226, Rennes F-35000, France. ⁶Univ Rennes, INSA Rennes, CNRS, Institut FOTON—UMR 6082, F-35000 Rennes, France. ✉e-mail: jacky.even@insa-rennes.fr; brahim.lounis@u-bordeaux.fr

for the development of quantum light sources^{11–13} and for spin-based technologies^{14–16}. The band-edge exciton of perovskites is expected to split by electron-hole exchange interaction into a dark ground singlet state (with zero angular momentum) and a bright triplet (with angular momentum unity)^{17–20}. However, since cesium lead halide perovskite nanocrystals (NCs) exhibit strong photoluminescence (PL) with triplet-line emission at cryogenic temperatures^{19,21–24}, it has been proposed that a Rashba effect reverses the fine structure level ordering and places the dark singlet above the bright triplet^{24–27}, making perovskites an exception among all bulk semiconductors and all existing semiconductor heterostructures. Studies on Mn-doped and undoped ensembles of CsPbCl₃ NCs²⁸ have suggested that the dark state is positioned below the bright triplet and that a slow bright–dark state relaxation at cryogenic temperatures gives rise to almost exclusively bright-state emission. Then, low-temperature single-NC magneto-optical spectroscopy²⁹ has provided direct signatures of the dark singlet exciton emission, showing that the singlet is positioned few meV below the bright triplet in hybrid organic–inorganic formamidinium lead bromide (FAPbBr₃)³⁰ and inorganic cesium lead iodide (CsPbI₃)⁹ NCs, in agreement with theoretical estimations of confined exchange interaction.

Similarly, no general picture is available for many-body Coulomb interactions in perovskites, besides investigations of the size

dependence of the biexciton and trion binding energies in single FAPbBr₃ NCs³¹. The biexciton binding energy has important consequences in the development of perovskite-based light-emitting technologies, since a large shift of the biexciton recombination lines with respect to those of the band-edge exciton would reduce the emission color purity under high-flux excitation. Its sign also fixes the transition that may sustain population inversion and NC gain for lasing applications³². For CsPbBr₃ perovskites, contradictory results have been reported on the amplitude and sign of the biexciton energy shift in the range –100 meV to 100 meV, using time- and spectrally- resolved PL^{33–35}, transient absorption^{36–39} or nonlinear⁴⁰ spectroscopic methods on NC ensembles. Heralded single-NC spectroscopy on CsPbBr₃ and CsPbI₃ perovskites lead to estimations of the biexciton binding energy at room-temperature with inherently low spectral precision and even uncertainties on the sign of the interaction⁴¹.

Here, we use low-temperature single-NC magneto-optical spectroscopy to reveal the entire band-edge exciton fine structure and charge-complex binding energies of nearly bulk CsPbBr₃ perovskite NCs, the reference materials for emerging applications and theoretical modeling. We demonstrate that the dark singlet exciton lays at least 3.6 meV below the bright triplet, at variance with the models based on the Rashba effect^{24–26}. This settles the debate on the bright-dark exciton level ordering in halide perovskite nanostructures. Moreover, the spectral fingerprint of biexciton recombination is also evidenced in these materials and provides precise measurements of the biexciton binding energy. Importantly, we show evidence for universal scaling laws that relate the exciton fine structure splitting, the trion and biexciton binding energies to the band-edge exciton energy in lead-halide perovskite nanostructures. For that purpose, we combine the present results on CsPbBr₃ single NCs with spectroscopic data on various perovskite NCs previously investigated^{9,21,22,24,30,31,42}. Additional measurements on single CsPb(Cl_xBr_{1–x})₃ NCs further extend the validity of these dependences over a broader emission spectral range. These scaling laws solely based on quantum confinement effects and dimensionless energies offer a general predictive picture for the interaction energies within charge complexes photo-generated in lead halide perovskites, regardless of their chemical composition.

Results

Tailoring nearly-bulk CsPbBr₃ NCs

Magnetic brightening of the dark exciton state is challenging in CsPbBr₃ perovskite NCs. Indeed, the PL intensity of the dark state is inversely proportional to the square of the bright-dark energy splitting, while the bulk electron-hole exchange interaction in this material is particularly strong among lead-halide perovskites⁹. Moreover, confinement effects in NCs enhance the exciton fine structure splittings, which makes magnetic brightening of the dark singlet even more difficult. The CsPbBr₃ NCs specifically prepared for this study are cuboids with sides that largely exceed the bulk exciton Bohr radius $a_B \sim 3.1$ nm in order to minimize quantum confinement effects on the dark-bright exciton splittings. These large NCs are synthesized under ambient conditions with the ligand-assisted reprecipitation approach, using a novel ligand molecule, oleylguanidinium bromide (OGB), to obtain dispersible and large CsPbBr₃ perovskite NCs (See Methods, Supplementary Figs. 1 and 2 for details of the NC synthesis and characterization). The 3D size and shape of these OGB-capped CsPbBr₃ NCs with orthorhombic crystal phase are characterized using 45°-tilted scanning electron microscopy (Fig. 1a). With average base lengths 195 ± 18 nm, 41 ± 8.5 nm and a thickness of ~ 40 nm, these NCs are nearly bulk-like particles with reduced quantum confinement. The ensemble absorption spectrum presents a threshold at ~ 520 nm (inset Fig. 1b), which roughly

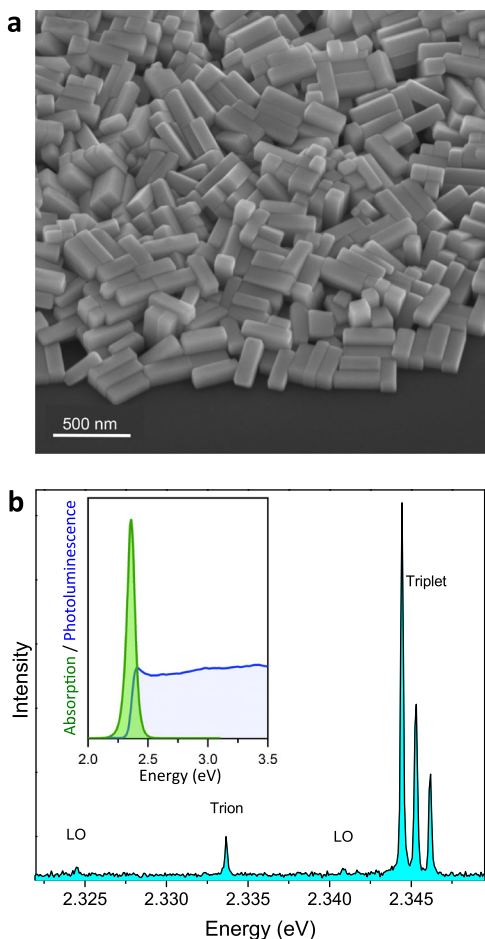


Fig. 1 | Characterization of the large OGB-capped CsPbBr₃ NCs. **a** 45°-Scanning electron microscopy image of the OGB-capped CsPbBr₃ NCs. Their room-temperature absorption and emission spectrum is shown in the inset of **b**. **b** Representative PL spectrum of a single NC at 3.5 K under laser excitation with wavelength 488 nm and intensity 50 W cm^{–2} (integration time 10 s). It displays the bright exciton triplet ZPLs, the trion recombination line as well as longitudinal optical (LO) phonon replicas.

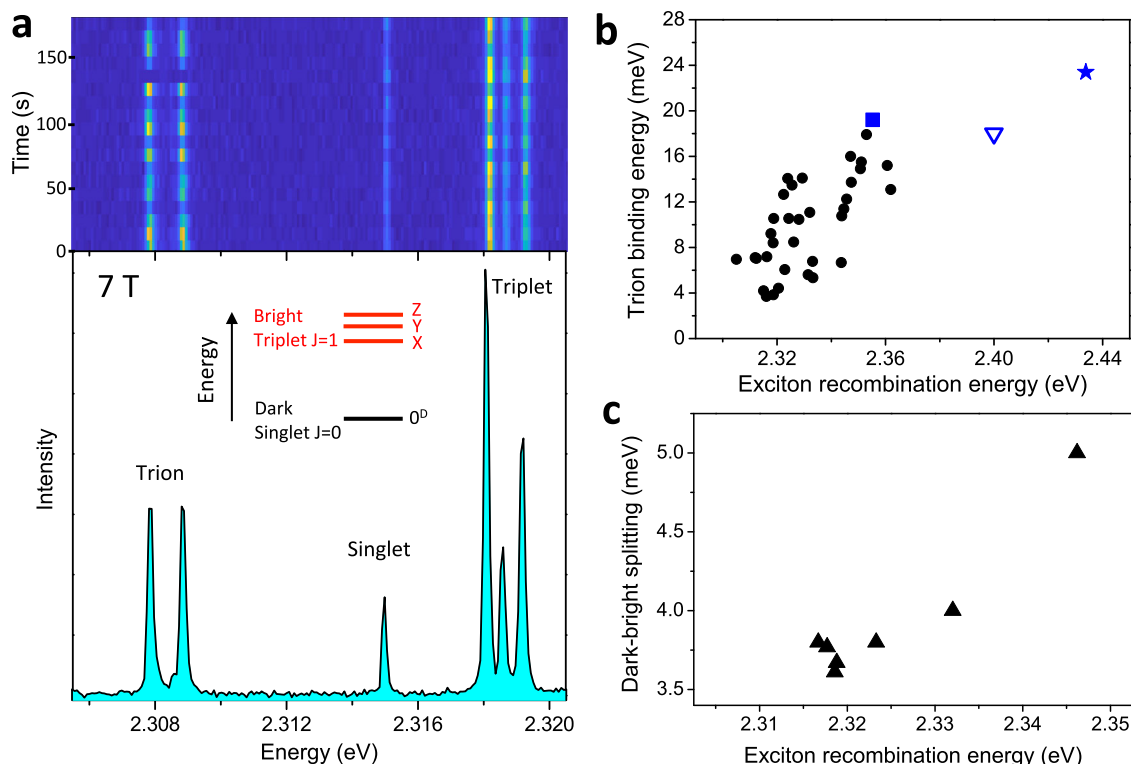


Fig. 2 | Band-edge exciton fine structure and trion binding energy in CsPbBr₃ NCs.

a The upper panel shows the spectral trail of a single NC at 7 T, showing switches between the entire exciton fine structure manifold (triplet + singlet) and the trion Zeeman doublet. The singlet and triplet lines clearly undergo identical variations of their PL intensities. The intensity variations of the doublet and the exciton manifold are anti-correlated, showing evidence that they belong to different charge complexes of the same NC. The lower panel displays the spectrum integrated over the spectral trail. The inset indicates the band-edge exciton fine-structure sublevels,

where X, Y, Z arbitrarily refer to linear and orthogonal emission dipoles associated with the NC axes. **b** Distribution of trion binding energies in CsPbBr₃ single NCs as a function of the exciton recombination energy taken at the central triplet ZPL. The black dots correspond to nearly-bulk NCs, the blue triangle to 9 nm sized NCs²¹. The blue star and the blue square respectively correspond to 5.5 nm sized and 14.5 nm sized NCs (Supplementary Fig. 5). **c** Dark-bright exciton splittings of nearly-bulk CsPbBr₃ NCs as a function of the exciton recombination energy.

corresponds to the room-temperature bulk electronic bandgap. Under light excitation at 405 nm, these NCs exhibit a bright green PL centered at 2.36 eV, with a high color purity (full width at half-maximum, FWHM, of 77 meV) and a PL quantum yield of 32 % (see inset Fig. 1b).

Band-edge exciton fine structure

At low temperature (3.5 ± 0.3 K) and under continuous-wave laser excitation with a wavelength of 488 nm (2.54 eV), the PL spectra of single NCs are characterized by a triplet of resolution-limited zero-phonon lines (ZPLs) corresponding to the recombination of the bright triplet exciton, followed by optical phonon replica, as exemplified on Fig. 1b. The photon energy of these recombination lines is distributed in the range 2.3–2.35 eV, i.e. across the low-temperature electronic bandgap $E_{\text{gap}} = 2.342$ eV of bulk CsPbBr₃⁴³. The spread of emission energies among the nearly-bulk CsPbBr₃ NCs may be due to stochastic deviations of cation positions or torsions of the halogen octahedra, which translate into a complex potential landscape felt by the exciton. This is a consequence of the very strong lattice anharmonicity or intrinsic polymorphous nature of the perovskite structure^{44–46}. In order to get an overview on the general consequences of these fluctuations, a theoretical framework is proposed in Supplementary Note 1 to show the smearing of the electronic density of states, which leads to the broadening of the energy distribution of the emission lines.

All triplets observed in this study are non-degenerate, which is consistent with triplet splittings mainly set by the NC anisotropic crystal phase for such large crystals^{21,47,48}. Indeed, the triplet splittings between extreme lines range from 0.5 to 2.3 meV (Supplementary

Fig. 3), with an average of -1.2 meV that matches the theoretical estimations for nearly-bulk CsPbBr₃ NCs with an orthorhombic crystal structure⁴⁸. One can also notice on Supplementary Fig. 3 that the triplet splittings have a slight correlation with the NC emission energies, which points to residual effects of exciton quantum confinement. The observation of triplet emission in perovskite NCs indicates that acoustic-phonon-assisted relaxation between triplet sublevels is much longer than the exciton recombination lifetime⁴⁹. This is due to the strong lattice anharmonicity in these soft materials, where the acoustic vibrational density of states is that of a glassy state.⁵⁰

For most of the NCs, the emission switches over time between the neutral exciton triplet and trion emission characterized by a single, red-shifted ZPL that invariably splits into two Zeeman components under the application of an external magnetic field, as shown in Fig. 2a. The *g*-factor associated with the trion doublet is narrowly distributed around 2.4 (Supplementary Fig. 4). This value is in broad agreement with the sum of electron and hole *g*-factors measured on CsPbBr₃ crystals with time-resolved Kerr rotation⁵¹. It is also very similar to the trion *g*-factors measured for -10 nm sized CsPbBr₃ NCs²¹, FAPbBr₃ NCs³⁰ and CsPbI₃ NCs⁹. Overall, these results point to a nearly isotropic character of the magnetic response of charged perovskite NCs, regardless of their size and chemical composition. The red shift of the trion line from the central triplet line provides a measure of the trion binding energy and spans from 3 to 18 meV among the studied NCs (Fig. 2b). A correlation emerges between the trion binding energy and the exciton recombination energy (Fig. 2a). This correlation becomes obvious when adding to this set of data the trion binding energy measured on smaller CsPbBr₃ NCs having sizes 14.5 nm, 9 nm and

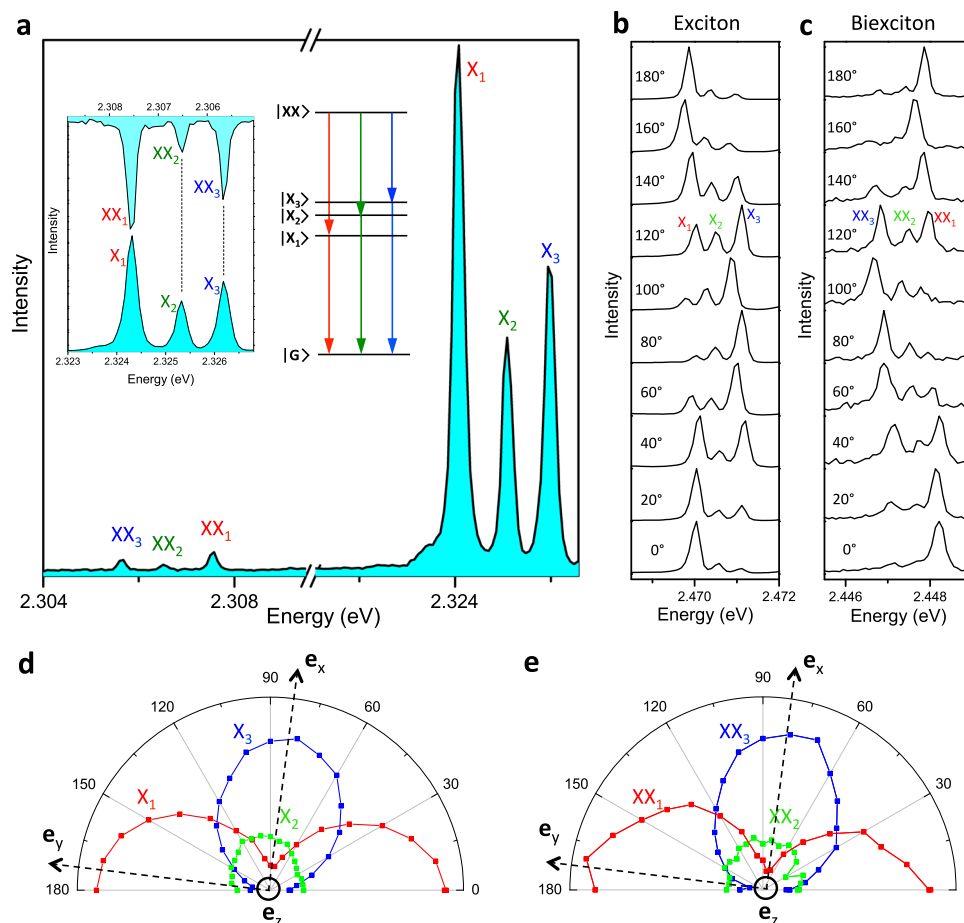


Fig. 3 | Biexciton-to-exciton transitions and biexciton binding energy in perovskite NCs. **a** Low-temperature PL spectrum of a single CsPbBr₃ NC at high excitation intensity (50 kW cm⁻²) and 7 T. The lines named X₁, X₂, X₃ are assigned to the exciton triplet recombination ZPLs. The red-shifted lines named XX₁, XX₂, XX₃ are assigned to the biexciton-to-exciton transitions and perfectly map onto the exciton triplet ZPLs under mirror image (left inset), allowing a straightforward correspondence of the transition lines (right inset). The spectral trail of this NC over time is shown in Supplementary Fig. 9. **b**, **c** Polarized PL spectra zoomed on the

exciton triplet ZPLs (**b**) and the biexciton recombination ZPLs (**c**) for a single CsPb(Cl_xBr_{1-x})₃ single NC with x=0.3 and size ~30 nm, for various analyzer angles ranging from 0° to 180°. The whole series of spectra is displayed in Supplementary Fig. 12. The evolutions of the exciton and biexciton ZPL-intensities as a function of the polarizer angle are displayed in the polar plots **d** and **e**, respectively. These polar plots are remarkably similar, demonstrating that X₁ and XX₁, X₂ and XX₂, X₃ and XX₃ have identical transition dipole orientations nearly aligned along the orthogonal unit vectors **e_y**, **e_z**, **e_x**, respectively.

5.5 nm (Fig. 2b). Their corresponding low-temperature emission energies are respectively 2.355 eV, ~2.40 eV²¹ and 2.434 eV, as a signature of increasing charge-carrier confinement.

Bright triplet–dark singlet level ordering

The application of a magnetic field also reveals the entire band-edge exciton fine structure of the nearly-bulk CsPbBr₃ NCs, as shown in Fig. 2a. While the triplet further splits under increasing fields, a red-shifted line indeed develops in the PL spectrum as a hallmark of magnetic brightening of the ground dark singlet exciton state (See also Supplementary Fig. 6). The ZPL of the dark state at fields limited to 7 T is often very weak and its observation requires PL spectra with a remarkable quality, which requires excellent photostability and long acquisitions times. The dark singlet lays 3.6 meV to 5 meV below the middle bright triplet sublevel in these CsPbBr₃ NCs (Fig. 2c). These results invalidate recent models of exciton fine structure, which predict for weakly confined CsPbBr₃ NCs a bright-dark exciton level inversion caused by the Rashba effect^{24–26}. The strong triplet luminescence of lead halide bulk-like perovskites NCs at liquid helium temperatures is actually a signature of reduced phonon-assisted relaxation to the dark ground exciton, even if the dark-bright splittings coincides with the LO-phonon energies.

Triplet-to-singlet relaxation with a LO-phonon is indeed inhibited due to the fact that phonons do not carry angular momentum^{52,53}. The ground singlet exciton can nevertheless be populated by relaxation from high-energy continuum states excited at 2.54 eV, with important consequences on the statistics of photons emitted by individual bulk-like NCs. As a matter of fact, strong photon bunching is evidenced in the low-temperature PL intensity auto-correlation function of these NCs (Supplementary Fig. 7), while a flat correlation is expected for bulk-like particles with Poissonian photon statistics. Magnetic coupling of dark and bright states leads to shortening of the long component of the PL decay and to weakening of the photon bunching, as shown in Supplementary Fig. 7 and modeled in Supplementary Fig. 8. These observations indicate that the population of the long-lived ground exciton state favors the formation of biexcitons in perovskites⁹.

Biexciton binding energy

Our spectroscopic investigations of single perovskite NCs also reveal the spectral fingerprint of the biexciton-to-exciton transitions. Indeed, raising the excitation intensity leads to the onset of a spectral triplet (XX) that is red-shifted with respect to the exciton (X) bright triplet (Fig. 3a), and whose temporal variations in PL intensity are correlated with those of the X triplet (Supplementary Fig. 9). Moreover, the ratio

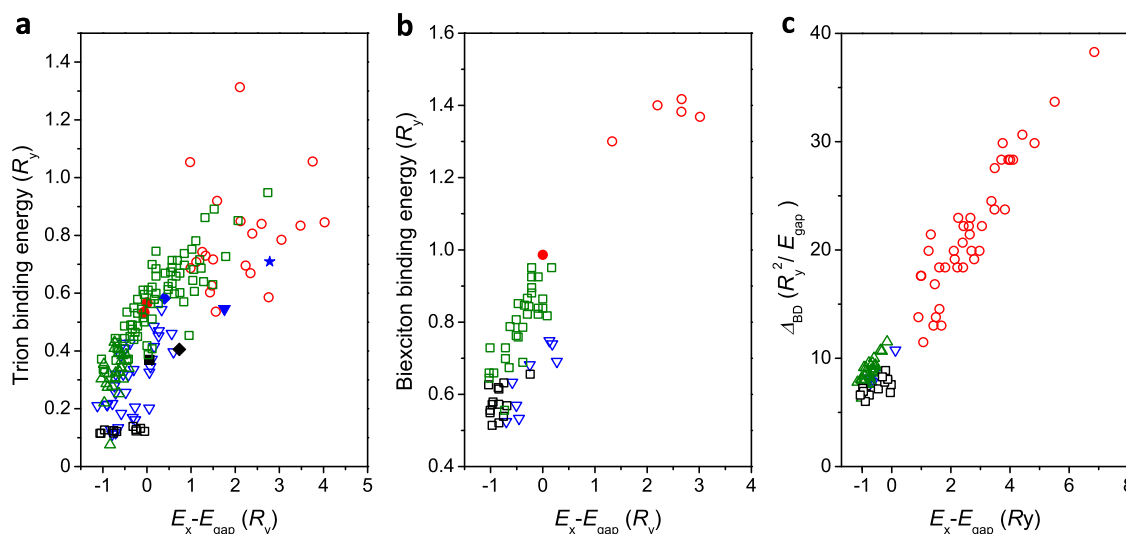


Fig. 4 | Scaling laws of charge-complex energies in lead-halide perovskite single NCs. Evolutions of the single-NC trion binding energies in R_y units (**a**), biexciton binding energies in R_y units (**b**) and dark-bright exciton energy splittings in R_y^2/E_{gap} units (**c**) as a function of the exciton recombination energy expressed in R_y units after bandgap subtraction. The splittings and binding energies are measured with respect to the central line of the exciton triplet. Open blue triangles: CsPbBr₃ NCs; Open black squares: CsPb(Cl_xBr_{1-x})₃ NCs; Green triangles: FAPbBr₃ NCs³⁰; Red circles: CsPbI₃ NCs⁹; Green squares: FAPbBr₃ NCs (data extracted from ref. ³¹). Plain blue triangle in (**a**): average data for 9 nm sized CsPbBr₃ NCs²¹. Blue star in (**a**): CsPbBr₃ NC with 5.5 nm size. Blue diamond in (**a**): CsPbBr₃ NC with 14.5 nm size. Plain black square in (**a**): CsPbClBr₂ NCs from ref. ²⁴. Black diamond in (**a**): CsPb(ClBr)₃ NCs from ref. ⁴². Red disks in (**a**) and (**b**): CsPbI₃ NCs²². For these

perovskites, the low-temperature bandgaps and bulk exciton binding energies taken for the normalization are deduced from refs. ^{43,62,63} (See Supplementary Table 1): $E_{\text{gap}} = 2.342$ eV and $R_y = 33$ meV for CsPbBr₃, $E_{\text{gap}} = 1.723$ eV and $R_y = 15$ meV for CsPbI₃, $E_{\text{gap}} = 2.233$ eV and $R_y = 24$ meV for FAPbBr₃, $E_{\text{gap}} = 2.513$ eV and $R_y = 42$ meV for CsPb(Cl_xBr_{1-x})₃ with $x = 0.24$. This value of x was adjusted using empirical interpolations of the bandgaps of bulk CsPbCl₃ and CsPbBr₃ materials composing the alloy. It matches reasonably well the estimation $x = 0.3$ after the growth procedure (see Methods). The trion binding energies in **a** experience a larger spread than the biexciton ones in **b**, as a result of spectral jumps accompanying the neutral-to-charged switches of the NCs, as illustrated in Supplementary Fig. 9.

of the integrated intensities of the XX and X triplets is proportional to the intensity of the X triplet, as a distinctive signature of XX biexciton emission^{22,54} (Supplementary Fig. 10). Additionally, the XX triplet components XX_{*i*} perfectly match the X triplet components X_{*i*} (*i* = 1, 2, 3) under mirror symmetry and are attributed to the three transitions that link the ground zero-angular-momentum biexciton state to the bright exciton triplet sublevels (Fig. 3a). Further evidence of the correspondence between the XX_{*i*} and X_{*i*} lines comes from their polarizations, as shown on Fig. 4b–e for another perovskite NC. For this NC, the transition dipoles associated to X₁ and X₃ (as well as XX₁ and XX₃), have nearly linear and orthogonal polarizations in the focal plane, while X₂ (as well as XX₂) with weak intensity and polarization character is assigned to a transition dipole oriented along the optical axis. This demonstrates that XX_{*i*} and X_{*i*} transitions involving the same bright state have identical polarizations, as expected from symmetry considerations (Supplementary Note 2).

Importantly, the red shift of the XX triplet with respect to the X triplet indicates that the biexciton interaction is attractive. In the large CsPbBr₃ particles, the biexciton binding energy ranges from 17 to 25 meV with a trend of correlation with the corresponding exciton recombination energy (Supplementary Fig. 11), as in the case of trion emission. These measurements provide the bulk CsPbBr₃ biexciton binding energy -17 meV, a key parameter for the development of refined models of many-body Coulomb interactions in perovskites⁵⁵. This value is in good agreement with that extrapolated from two-dimensional electronic spectroscopic measurements performed on small CsPbBr₃ NC ensembles⁴⁰.

In order to strengthen the generality of these findings, we have also conducted magneto-optical spectroscopic investigations of mixed-halide CsPb(Cl_xBr_{1-x})₃ single NCs with an average size ~30 nm (See Methods). These perovskites follow the same behaviors as the other compounds in terms of exciton sublevel ordering and signs of the interactions within trion and biexciton charge complexes. Their

exciton dark-bright splittings are found in the range 4–6 meV, while their trion and biexciton binding energies are respectively of the order of 5 meV and 24 meV (Supplementary Fig. 13).

Discussion

We now aim at giving a general and predictive picture for the exciton dark-bright energy splittings as well as the trion and biexciton binding energies in lead halide perovskite NCs from various compositions, on the basis of single-NC spectroscopic data gathered in this study and from previous reports^{9,21,22,24,30,31,42}. As compared to II–VI and III–V semiconductor, perovskites exhibit a simpler band structure (a single valence band, and a single conduction band due to the giant spin-orbit coupling). Moreover, for each perovskite compound, the electron and the hole have nearly identical and effective masses m^* ^{18,24} and confinement potentials. The Hamiltonian \mathcal{H} describing the kinetic and Coulomb energies of the charge carriers in a NC, where the confinement potential with infinitely high barriers is taken to zero, can be written

$$\mathcal{H} = \sum_A \frac{-\hbar^2}{2m^*a_B^2} \frac{1}{(L_{\text{eff}}/a_B)^2} \hat{\nabla}_A^2 + \sum_{A<B} \frac{e^2}{4\pi\epsilon_0\epsilon a_B} \frac{c_A c_B}{(L_{\text{eff}}/a_B)} \frac{1}{|\hat{\mathbf{r}}_A - \hat{\mathbf{r}}_B|} \quad (1)$$

$$= R_y \left(\sum_A \frac{-1}{2(L_{\text{eff}}/a_B)^2} \hat{\nabla}_A^2 + \frac{2}{(L_{\text{eff}}/a_B)} \sum_{A<B} c_A c_B \frac{1}{|\hat{\mathbf{r}}_A - \hat{\mathbf{r}}_B|} \right)$$

where L_{eff} is the effective NC confinement size, $\hat{\nabla}_i$ and $\hat{\mathbf{r}}_i$ the dimensionless (normalized to L_{eff}) Nabla-operators and coordinates of the charge carriers *i* (*i* = A, B...), c_i the signs of their charges having absolute value e , and $R_y = \hbar^2/(m^*a_B^2)$ the bulk exciton Rydberg energy, ϵ being the perovskite dielectric constant. Such normalization in Rydberg's units makes interaction energies independent of the material and shows that trion and biexciton binding energies are essentially set by the quantum confinement regime, i.e. the

dimensionless ratio $L_{\text{eff}}/a_{\text{B}}$. This simple statement explains the universal laws relating in Rydberg's units the experimental trion and biexciton binding energies to the exciton recombination energy E_{X} , once the bandgap of the material is subtracted (Fig. 4a, b). Indeed, using these scales, the experimental points strikingly spread along a trend line from the bulk limit (abscissa approaching -1) to the strong confinement regime (abscissa of several units), regardless of the perovskite compositions.

The dark-bright exciton energy splitting Δ_{BD} measured on single NCs of CsPbBr_3 , $\text{CsPb}(\text{Cl}_x\text{Br}_{1-x})_3$, CsPbI_3 ⁹ and FAPbBr_3 ³⁰ also displays a universal scaling law as a function of the exciton quantum confinement. This splitting mainly set by the long-range contribution of the exchange interaction is directly related to the energy difference between longitudinal and transverse excitons in bulk semiconductors, which is proportional to $R_{\text{y}}^2/E_{\text{gap}}$ (Supplementary Note 1). Adding the short-range contribution²⁰, we show in the Supplementary Table 2 that the total exchange interaction expected for bulk perovskites with various compositions converge to nearly equal values, once normalized with $R_{\text{y}}^2/E_{\text{gap}}$. Moreover, the short-range and long-range contributions of the exchange interaction are predicted to have the same NC size-dependence in the strongly confined regime⁵⁶. We have thus plotted the normalized splittings $\Delta_{\text{BD}}/(\frac{R_{\text{y}}^2}{E_{\text{gap}}})$ of all these NCs as a function of the corresponding exciton recombination energies in Rydberg's units, after bandgap subtraction (Fig. 4c). This figure shows evidence that the data points line up on a same curve, regardless of the cation and halide contained in the perovskite.

Overall, the dimensionless experimental dark-bright exciton splittings as well as trion and biexciton binding energies are evidenced to display a universal behavior mainly set by the quantum confinement of the charge carriers in perovskite nanostructures, without the need for prior characterization of the NC size or composition. Beyond settling the debate on the bright and dark exciton sublevel ordering and its main origin in lead halide perovskites, the laws unraveled by single-NC spectroscopy offer a general predictive picture for the interaction energies within charge complexes photo-generated in these materials. They also pave the way to the development of accurate models of charge complex interactions in lead halide perovskites, which share common physics and form a unique class of semiconductors.

Methods

Synthesis of N-(octadec-9-en-1-yl)guanidinium hydrobromide (oleylguanidinium bromide, OGB) ligands

Oleylamine (1 eq) was added to S-ethylisothiurea hydrobromide (1.2 eq) suspended in tetrahydrofuran (THF). The resulting mixture was stirred at room temperature overnight. Then THF was evaporated under reduced pressure and the resulting residue was recrystallized with diethylether (Et_2O). The obtained precipitate was washed several times with Et_2O and dried under reduced pressure overnight at 50°C .

N-(octadec-9-en-1-yl)guanidinium hydrobromide (3, OGB). Yield 60%; white solid. ^1H NMR (400 MHz, DMSO) δ , ppm (*J*, Hz): 7.48 (t, *J* = 5.6 Hz, 1H), 7.20 (s, 2H), 6.86 (s, 1H), 5.34 (dt, *J* = 14.7, 4.3 Hz, 1H), 3.09 (q, *J* = 6.6 Hz, 1H), 1.98 (q, *J* = 6.1 Hz, 1H), 1.93 (t, *J* = 5.8 Hz, 1H), 1.44 (q, *J* = 7.0 Hz, 2H), 1.25 (d, *J* = 9.5 Hz, 18H), 0.86 (s, 1H), 0.86 (d, *J* = 13.5 Hz, 1H). ^{13}C NMR (101 MHz, DMSO) δ , ppm: 157.19; 130.54; 130.51; 130.11; 130.07; 41.20; 32.41; 31.75; 29.60; 29.56; 29.52; 29.47; 29.44; 29.32; 29.29; 29.18; 29.16; 29.08; 29.06; 28.94; 28.91; 27.08; 27.04; 26.52; 22.56; 14.41.

The structural formula of OGB is displayed in Supplementary Fig. 1.

Ligand-assisted-precipitation synthesis of OGB-capped CsPbBr_3 nanocrystals

The hybrid precursor solution was prepared by mixing solutions of 90 μL of PbBr_2 (0.67 M in DMF), 465 μL of CsBr (0.043 M in

DMF-DMSO in ratio 1:1) and 300 μL of OGB (1 M in DMF), where DMF denotes dimethyl formamide and DMSO dimethyl sulfoxide. 75 μL of the hybrid precursor solution was injected into a 4 mL vial containing 2.5 mL of vigorously stirred mesitylene to initiate fast nucleation of the CsPbBr_3 NRs. The green solution with bright green luminescence could be observed in 15–20 s. For purification of the CsPbBr_3 NCs, 0.25 mL of ethyl acetate was added to 0.5 mL of the crude solution, followed by centrifugation for 4 min at $4250 \times g$. The supernatant was discarded and the precipitate was dispersed in 0.4 mL of toluene.

The synthesis and characterization of the OGB-capped CsPbBr_3 NCs are depicted on Supplementary Fig. 2.

The solution of CsPbBr_3 NCs was then diluted 50 times into a solution of polystyrene (1 wt%) in toluene, and 25 μL of the resulting solution was spin-coated on a clean 1 cm x 1 cm sapphire substrate with a rotation speed of 2000 rpm for 60 s, for low-temperature magneto-optical spectroscopic measurements.

Synthesis of $\text{CsPb}(\text{Cl}_x\text{Br}_{1-x})_3$ NCs with $x=0.3$

$\text{CsPb}(\text{Br/Cl})_3$ NCs with size ~ 30 nm were prepared by partial anion-exchange of CsPbBr_3 NCs^{57,58}.

First, ~ 30 nm-sized CsPbBr_3 NCs were synthesized with the following modifications with respect to Ref. ⁵⁹. The injection of Cs-oleate and further annealing were conducted at 225°C . Such large CsPbBr_3 NCs were colloidal stabilized by lecithin as a capping ligand. While the reaction mixture was cooling down, at 50°C 2 mL of lecithin in toluene (0.01 M) were added and the solution was stirred for 30 min. The crude solution was centrifuged for 5 min at $1600 \times g$. The resulting supernatant was discarded and the precipitate was dispersed in a lecithin/toluene mixture (0.01 M, 2 mL) and kept undisturbed for 1 h. Then, the solution was centrifuged a second time for 4 min at $1600 \times g$. The precipitate was redispersed in toluene/1,2-dichlorobenzene (v/v 0.6:1).

The anion-exchange reaction was conducted at room temperature. As a source of chloride ions the mixture of didodecylmethylammonium chloride (DDAC)/ PbCl_2 in toluene was used. The solution of DDAC/ PbCl_2 in toluene was prepared by mixing 42 mg DDAC and 13.8 mg PbCl_2 with 7.5 mL toluene under moderate heating. 200 μL of CsPbBr_3 NC colloid prepared as described above were mixed with 6.5 μL of the DDAC/ PbCl_2 mixture.

An estimation $x \sim 0.3$ for the relative amount of chloride atoms in $\text{CsPb}(\text{Cl}_x\text{Br}_{1-x})_3$ NCs is derived from the empirical Vegard's law^{60,61}, using the room temperature bandgap of this alloy $E_{\text{gap}}(x) = 2.57$ eV measured from the absorption spectrum.

A TEM image of these NCs is presented in Supplementary Fig. 13.

Data availability

All data that support the conclusions of this study are included in the article and the Supplementary Information file. These data are available from the corresponding author upon request.

Code availability

Numerical codes used in this study are available from the corresponding author upon request.

References

- Kovalenko, M. V., Protesescu, L. & Bodnarchuk, M. I. Properties and potential optoelectronic applications of lead halide perovskite nanocrystals. *Science* **358**, 745–750 (2017).
- Yan, F., Tan, S. T., Li, X. & Demir, H. V. Light Generation in Lead Halide Perovskite Nanocrystals: LEDs, Color Converters, Lasers, and Other Applications. *Small* **15**, 1902079 (2019).
- Jena, A. K., Kulkarni, A. & Miyasaka, T. Halide Perovskite Photovoltaics: Background, Status, and Future Prospects. *Chem. Rev.* **119**, 3036–3103 (2019).

4. Kim, J. Y., Lee, J.-W., Jung, H. S., Shin, H. & Park, N.-G. High-Efficiency Perovskite Solar Cells. *Chem. Rev.* **120**, 7867–7918 (2020).
5. Park, Y.-S., Guo, S., Makarov, N. S. & Klimov, V. I. Room Temperature Single-Photon Emission from Individual Perovskite Quantum Dots. *ACS Nano* **9**, 10386–10393 (2015).
6. Hu, F. et al. Superior Optical Properties of Perovskite Nanocrystals as Single Photon Emitters. *ACS Nano* **9**, 12410–12416 (2015).
7. Rainò, G. et al. Superfluorescence from lead halide perovskite quantum dot superlattices. *Nature* **563**, 671–675 (2018).
8. Utzat, H. et al. Coherent single-photon emission from colloidal lead halide perovskite quantum dots. *Science* **363**, 1068–1072 (2019).
9. Tamarat, P. et al. The dark exciton ground state promotes photon-pair emission in individual perovskite nanocrystals. *Nat. Commun.* **11**, 1–8 (2020).
10. Feng, S. et al. Universal Existence of Localized Single-Photon Emitters in the Perovskite Film of All-Inorganic CsPbBr₃ Microcrystals. *Adv. Mat.* 2106278 (2021).
11. Lounis, B. & Orrit, M. Single-photon sources. *Rep. Prog. Phys.* **68**, 1129–1179 (2005).
12. Benson, O., Santori, C., Pelton, M. & Yamamoto, Y. Regulated and Entangled Photons from a Single Quantum Dot. *Phys. Rev. Lett.* **84**, 2513–2516 (2000).
13. Stevenson, R. M. et al. A semiconductor source of triggered entangled photon pairs. *Nature* **439**, 179–182 (2006).
14. Kim, M., Im, J., Freeman, A. J., Ihm, J. & Jin, H. Switchable $S = 1/2$ and $J = 1/2$ Rashba bands in ferroelectric halide perovskites. *PNAS* **111**, 6900–6904 (2014).
15. Zheng, F., Tan, L. Z., Liu, S. & Rappe, A. M. Rashba Spin–Orbit Coupling Enhanced Carrier Lifetime in CH₃NH₃PbI₃. *Nano Lett.* **15**, 7794–7800 (2015).
16. Kepenekian, M. et al. Rashba and Dresselhaus Effects in Hybrid Organic–Inorganic Perovskites: From Basics to Devices. *ACS Nano* **9**, 11557–11567 (2015).
17. Tanaka, K. et al. Comparative study on the excitons in lead-halide-based perovskite-type crystals CH₃NH₃PbBr₃ CH₃NH₃PbI₃. *Solid State Commun.* **127**, 619–623 (2003).
18. Even, J. Pedestrian Guide to Symmetry Properties of the Reference Cubic Structure of 3D All-Inorganic and Hybrid Perovskites. *J. Phys. Chem. Lett.* **6**, 2238–2242 (2015).
19. Ramade, J. et al. Fine structure of excitons and electron–hole exchange energy in polymorphic CsPbBr₃ single nanocrystals. *Nanoscale* **10**, 6393–6401 (2018).
20. Ben Aich, R., Ben Radhia, S., Boudjaria, K., Chammaro, M. & Testelin, C. Multiband k-p Model for Tetragonal Crystals: Application to Hybrid Halide Perovskite Nanocrystals. *J. Phys. Chem. Lett.* **11**, 808–817 (2020).
21. Fu, M. et al. Neutral and Charged Exciton Fine Structure in Single Lead Halide Perovskite Nanocrystals Revealed by Magneto-Optical Spectroscopy. *Nano Lett.* **17**, 2895–2901 (2017).
22. Yin, C. et al. Bright-Exciton Fine-Structure Splittings in Single Perovskite Nanocrystals. *Phys. Rev. Lett.* **119**, 026401 (2017).
23. Isarov, M. et al. Rashba Effect in a Single Colloidal CsPbBr₃ Perovskite Nanocrystal Detected by Magneto-Optical Measurements. *Nano Lett.* **17**, 5020–5026 (2017).
24. Becker, M. A. et al. Bright triplet excitons in caesium lead halide perovskites. *Nature* **553**, 189–193 (2018).
25. Sercel, P. C. et al. Exciton Fine Structure in Perovskite Nanocrystals. *Nano Lett.* **19**, 4068–4077 (2019).
26. Sercel, P. C., Lyons, J. L., Bernstein, N. & Efros, A. L. Quasicubic model for metal halide perovskite nanocrystals. *J. Chem. Phys.* **151**, 234106 (2019).
27. Swift, M. W., Lyons, J. L., Efros, A. L. & Sercel, P. C. Rashba exciton in a 2D perovskite quantum dot. *Nanoscale* **13**, 16769–16780 (2021).
28. Xu, K., Vliem, J. F. & Meijerink, A. Long-Lived Dark Exciton Emission in Mn-Doped CsPbCl₃. *J. Phys. Chem. C* **123**, 979–984 (2019).
29. Hou, L., Tamarat, P. & Lounis, B. Revealing the Exciton Fine Structure in Lead Halide Perovskite Nanocrystals. *Nanomaterials* **11**, 1058 (2021).
30. Tamarat, P. et al. The ground exciton state of formamidinium lead bromide perovskite nanocrystals is a singlet dark state. *Nat. Mater.* **18**, 717–724 (2019).
31. Cho, K. et al. Luminescence Fine Structures in Single Lead Halide Perovskite Nanocrystals: Size Dependence of the Exciton–Phonon Coupling. *Nano Lett.* **21**, 7206–7212 (2021).
32. Klimov, V. I. et al. Single-exciton optical gain in semiconductor nanocrystals. *Nature* **447**, 441–446 (2007).
33. Wang, Y. et al. All-Inorganic Colloidal Perovskite Quantum Dots: A New Class of Lasing Materials with Favorable Characteristics. *Adv. Mater.* **27**, 7101–7108 (2015).
34. Castañeda, J. A. et al. Efficient Biexciton Interaction in Perovskite Quantum Dots Under Weak and Strong Confinement. *ACS Nano* **10**, 8603–8609 (2016).
35. Shulenberger, K. E. et al. Setting an Upper Bound to the Biexciton Binding Energy in CsPbBr₃ Perovskite Nanocrystals. *J. Phys. Chem. Lett.* **10**, 5680–5686 (2019).
36. Makarov, N. S. et al. Spectral and Dynamical Properties of Single Excitons, Biexcitons, and Triions in Cesium–Lead-Halide Perovskite Quantum Dots. *Nano Lett.* **16**, 2349–2362 (2016).
37. Aneesh, J. et al. Ultrafast Exciton Dynamics in Colloidal CsPbBr₃ Perovskite Nanocrystals: Biexciton Effect and Auger Recombination. *J. Phys. Chem. C* **121**, 4734–4739 (2017).
38. Ashner, M. N. et al. Size-Dependent Biexciton Spectrum in CsPbBr₃ Perovskite Nanocrystals. *ACS Energy Lett.* **4**, 2639–2645 (2019).
39. Dana, J., Binyamin, T. & Ruhman, S. Unusually Strong Biexciton Repulsion Detected in Quantum Confined CsPbBr₃. *ACS Nano* **15**, 9039–9047 (2021).
40. Huang, X. et al. Inhomogeneous Biexciton Binding in Perovskite Semiconductor Nanocrystals Measured with Two-Dimensional Spectroscopy. *J. Phys. Chem. Lett.* **11**, 10173–10181 (2020).
41. Lubin, G. et al. Resolving the Controversy in Biexciton Binding Energy of Cesium Lead Halide Perovskite Nanocrystals through Heralded Single-Particle Spectroscopy. *ACS Nano* **15**, 19581–19587 (2021).
42. Rainò, G. et al. Single Cesium Lead Halide Perovskite Nanocrystals at Low Temperature: Fast Single-Photon Emission, Reduced Blinking, and Exciton Fine Structure. *ACS Nano* **10**, 2485–2490 (2016).
43. Yang, Z. et al. Impact of the Halide Cage on the Electronic Properties of Fully Inorganic Cesium Lead Halide Perovskites. *ACS Energy Lett.* **2**, 1621–1627 (2017).
44. Weadock, N. J. et al. Test of the Dynamic-Domain and Critical Scattering Hypotheses in Cubic Methylammonium Lead Triiodide. *Phys. Rev. Lett.* **125**, 075701 (2020).
45. Zhao, X.-G., Dalpian, G. M., Wang, Z. & Zunger, A. Polymorphous nature of cubic halide perovskites. *Phys. Rev. B* **101**, 155137 (2020).
46. Hehlen, B. et al. Pseudospin-phonon pretransitional dynamics in lead halide hybrid perovskites. *Phys. Rev. B* **105**, 024306 (2022).
47. Nestoklon, M. O. et al. Optical orientation and alignment of excitons in ensembles of inorganic perovskite nanocrystals. *Phys. Rev. B* **97**, 235304 (2018).
48. Ben Aich, R. et al. Bright-Exciton Splittings in Inorganic Cesium Lead Halide Perovskite Nanocrystals. *Phys. Rev. Appl.* **11**, 034042 (2019).
49. Fu, M. et al. Unraveling exciton–phonon coupling in individual FAPbI₃ nanocrystals emitting near-infrared single photons. *Nat. Commun.* **9**, 3318 (2018).
50. Miyata, K., Atallah, T. L. & Zhu, X.-Y. Lead halide perovskites: Crystal-field duality, phonon glass electron crystals, and large polaron formation. *Sci. Adv.* **3**, e1701469 (2017).

51. Belykh, V. V. et al. Coherent spin dynamics of electrons and holes in CsPbBr₃. *Nat. Commun.* **10**, 673 (2019).
52. Benny, Y., Presman, R., Poem, E. & Gershoni, D. Electron-hole spin flip-flop in semiconductor quantum dots. *Phys. Rev. B* **89**, 035316 (2014).
53. Wei, H., Guo, G.-C. & He, L. Slow exciton spin relaxation in single self-assembled In_{1-x}Ga_xAs/GaAs quantum dots. *Phys. Rev. B* **89**, 576 (2014).
54. Louyer, Y. et al. Efficient Biexciton Emission in Elongated CdSe/ZnS Nanocrystals. *Nano Lett.* **11**, 4370–4375 (2011).
55. Nguyen, T. P. T., Blundell, S. A. & Guet, C. Calculation of the biexciton shift in nanocrystals of inorganic perovskites. *Phys. Rev. B* **101**, 125424 (2020).
56. Goupalov, S. V. & Ivchenko, L. E. Electron-hole long-range exchange interaction in semiconductor quantum dots. *J. Cryst. Growth* **184/185**, 393–397 (1998).
57. Nedelcu, G. et al. Fast Anion-Exchange in Highly Luminescent Nanocrystals of Cesium Lead Halide Perovskites (CsPbX₃, X = Cl, Br, I). *Nano Lett.* **15**, 5635–5640 (2015).
58. Scharf, E. et al. Ligands Mediate Anion Exchange between Colloidal Lead-Halide Perovskite Nanocrystals. *Nano Lett.* **7**, 10775–10981 (2022).
59. Bera, S., Behera, K. & Pradhan, N. α -Halo Ketone for Polyhedral Perovskite Nanocrystals: Evolutions, Shape Conversions, Ligand Chemistry, and Self-Assembly. *J. Am. Chem. Soc.* **142**, 20865–20874 (2020).
60. Liaschenko, T. G. et al. Electronic structure of CsPbBr_{3-x}Cl_x perovskites: synthesis, experimental characterization, and DFT simulations. *Phys. Chem. Chem. Phys.* **21**, 18930–18938 (2019).
61. Hossain, M. K. et al. Controllable optical emission wavelength in all-inorganic halide perovskite alloy microplates grown by two-step chemical vapor deposition. *Nano Res.* **13**, 2939–2949 (2020).
62. Galkowski, K. et al. Determination of the exciton binding energy and effective masses for methylammonium and formamidinium lead trihalide perovskite semiconductors. *Energy Environ. Sci.* **9**, 962–970 (2016).
63. Baranowski, M. et al. Exciton binding energy and effective mass of CsPbCl₃: a magneto-optical study. *Photonics Res.* **8**, A50–A55 (2020).

Acknowledgements

We acknowledge the financial support from the French National Agency for Research, Région Aquitaine, Idex Bordeaux (Research Program GPR Light), and the EUR Light S&T, as well as funds from the European Union's Horizon 2020 program, through a FET Open research and innovation action under the grant agreement No 899141 (PoLLoC). J.E. and B.L. acknowledge the Institut universitaire de France. M.I.B. thanks support by the Swiss National Science Foundation (grant number 200021_192308, project Q-Light). Y.B., M.V.K., M.I.B. acknowledge

support by the Research and Innovation Foundation of Cyprus (Program “New Strategic Infrastructure Units-Young Scientists”, grant “INFRA-STRUCTURES/1216/0004”, Acronym “NANOSONICS”). We thank Yevhen Shynkarenko for the absorption measurement used in Fig. 1, and are grateful for the use of facilities of the Empa Electron Microscopy Center.

Author contributions

Y.B., A.M., M.I.B. and M.V.K. prepared the samples and performed the ensemble characterization. P.T., E.P., C.X., L.H. and J.B.T. performed the optical experiments. P.T., J.E. and B.L. analyzed and interpreted the data. T.P.T.N., M.Z., L.P., C.K. and J.E. developed the theoretical models. P.T., J.E. and B.L. wrote the manuscript with inputs from all authors. B.L. supervised the project.

Competing interests

The authors declare no competing interests.

Additional information

Supplementary information The online version contains supplementary material available at <https://doi.org/10.1038/s41467-023-35842-4>.

Correspondence and requests for materials should be addressed to Jacky Even or Brahim Lounis.

Peer review information *Nature Communications* thanks the anonymous reviewer(s) for their contribution to the peer review of this work.

Reprints and permissions information is available at <http://www.nature.com/reprints>

Publisher's note Springer Nature remains neutral with regard to jurisdictional claims in published maps and institutional affiliations.

Open Access This article is licensed under a Creative Commons Attribution 4.0 International License, which permits use, sharing, adaptation, distribution and reproduction in any medium or format, as long as you give appropriate credit to the original author(s) and the source, provide a link to the Creative Commons license, and indicate if changes were made. The images or other third party material in this article are included in the article's Creative Commons license, unless indicated otherwise in a credit line to the material. If material is not included in the article's Creative Commons license and your intended use is not permitted by statutory regulation or exceeds the permitted use, you will need to obtain permission directly from the copyright holder. To view a copy of this license, visit <http://creativecommons.org/licenses/by/4.0/>.

© The Author(s) 2023